Assessment of Thermal Transport Properties of Group-III Nitrides: A Classical Molecular Dynamics Study with Transferable Tersoff-Type Interatomic Potentials

Yenal Karaaslan[1], Haluk Yapicioglu[2], and Cem Sevik[1,*]

[1]*Department of Mechanical Engineering, Eskişehir Technical University, 26555 Eskişehir, Turkey*
[2]*Department of Industrial Engineering, Eskişehir Technical University, 26555 Eskişehir, Turkey*

In this study, by means of classical molecular dynamics simulations, we investigate the thermal-transport properties of hexagonal single-layer, zinc-blend, and wurtzite phases of BN, AlN, and GaN crystals, which are very promising for the application and design of high-quality electronic devices. With this in mind, we generate fully transferable Tersoff-type empirical interatomic potential parameter sets by utilizing an optimization procedure based on particle-swarm optimization. The predicted thermal properties as well as the structural, mechanical, and vibrational properties of all materials are in very good agreement with existing experimental and first-principles data. The impact of isotopes on thermal transport is also investigated and between approximately 10 and 50% reduction in phonon thermal transport with random isotope distribution is observed in BN and GaN crystals. Our investigation distinctly shows that the generated parameter sets are fully transferable and very useful in exploring the thermal properties of systems containing these nitrides.

I. INTRODUCTION

Over the past three decades, the binary group-III-nitride semiconductors, in particular GaN, AlN, and their alloys have attracted an extraordinary amount of interest due to their usability in electronic and optoelectronic device applications, requiring high efficiency at short wavelengths, high operation temperatures, high powers, and high frequencies [1–6]. Therefore, these materials have been studied extensively and their superior physical properties, such as wide band gap, high thermal conductivity, short bond length, high dielectric constant, and low compressibility, has been emphasized as the prominent characteristics of these crystals [7–14]. These peculiar properties have provided this material family with various application domains such as high electron mobility transistors, laser diodes, light-emitting diodes, photodetectors, solar cells, electro-optic modulators, and biosensors [15–20]. Typically, these extraordinary materials grow in the *wurtzite* crystal structure where atoms are fourfold coordinated adopting sp^3 hybridization. However, with the recent advances in fabrication technologies, the low-dimensional graphenelike (threefold coordinated adopting sp^2 hybridization) structures of BN [21–26], AlN [27,28], and GaN [29,30] have been successfully fabricated with high dimensional accuracy. And research studies on the

investigation of the capability of these materials with regard to future device applications, particularly to address desired factors of high computing performance, low power consumption, cool operation, and lightweight have begun to appear in the literature [31–34].

Similar to their bulk counterparts, adopting this material family for future device technologies is quite probable. Therefore, the accurate characterization of particularly device-related physical properties of these crystals is of utmost importance. For instance, thermal-transport properties that provide a basis for thermal energy control and thermal management of electronic and optoelectronic devices needs to be systematically investigated. In fact, efficient thermal management is required to cope with the problem of excess heat that occurs in conjunction with the efforts to miniaturize devices and improve their performance parameters. Indeed, this is directly related to the understanding of thermal-transport properties of materials used in device fabrication.

One of the best approaches to investigate the thermal-transport properties of materials regarding device applications is classical molecular dynamics (CMD) simulations due to the fact that it is suitable to investigate large-scale systems in the order of millions of atoms. CMD simulations have proven to generate highly accurate results for thermal-transport properties of bulk and nanostructures, including disorders such as grain boundary, vacancy, and isotope defects [35–39]. However, CMD simulations

---

*csevik@eskisehir.edu.tr

require an accurate empirical interatomic potential (EIAP) generated specifically aiming at the desired physical properties. In the case of thermal-transport properties, accurate description of atomic vibrations is essential. Also, transferability of the generated EIAP is highly critical to investigate material considered in its different crystal structures. An accurate transferable EIAP is crucial not only in the development of heat-control mechanisms for electronic device applications such as information, communication, and energy-storage technologies [40–42], but also in nanostructure device application simulations, such as drug delivery, superlubricity, and thermal rectification [43–45].

In this study, we first optimize a Tersoff-type EIAP parameter set for binary group-III-nitride compounds, BN, AlN, and GaN, and we systematically investigate the lattice thermal-transport properties of these materials. The generated parameter sets for each material are proven to accurately describe structural, mechanical, dynamical as well as thermal-transport properties. In addition, considering different three-body parameter sets, i.e., B-N-N, and N-B-B, vacancy defect energies are generated in high accuracy. The transferability of the generated parameters is demonstrated by systematically testing on hexagonal single-layer, zinc-blend, and wurtzite structures. Our results indicate that isotope disorder has a strong influence on thermal-transport properties of BN and GaN crystals.

II. COMPUTATIONAL METHODS AND DETAILS

The form of considered three-body Tersoff interatomic potential [46] for the energy, E of a system of atoms is expressed as follows:

$$E = \frac{1}{2} \sum_i \sum_{j \neq i} V_{ij} \tag{1}$$

$$V_{ij} = f^C(r_{ij}) \left[a_{ij} f^R(r_{ij}) - b_{ij} f^A(r_{ij}) \right],$$

$$f^C(r) = \begin{cases} 1, & r < R - D \\ \frac{1}{2} - \frac{1}{2} \sin\left[\frac{\pi}{2}\frac{(r-R)}{D}\right], & R - D < r < R + D \\ 0, & r < R + D \end{cases}$$

$$f^R(r) = A \exp(-\lambda_1 r),$$

$$f^A(r) = B \exp(-\lambda_2 r),$$

$$a_{ij} = \left(1 + \alpha^n \eta_{ij}^n\right)^{-1/2n},$$

$$b_{ij} = \left(1 + \beta^n \xi_{ij}^n\right)^{-1/2n},$$

$$\xi_{ij} = \sum_{k \neq i,j} f^C(r_{ik}) g(\theta_{ijk}) \exp\left[\lambda_3^3 (r_{ij} - r_{ik})^3\right],$$

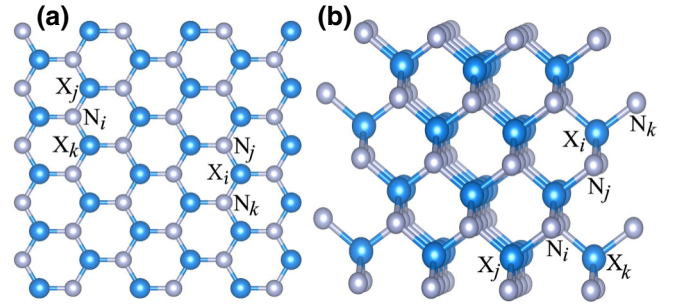$$g(\theta_{ijk}) = 1 + \frac{c^2}{d^2} - \frac{c^2}{d^2 + (h - \cos\theta_{ijk})^2}. \tag{2}$$

FIG. 1. Schematic representation of the group-III-nitride crystal structures (X = boron, aluminum, gallium; N = nitrogen; i is the central atom, j and k are two neighbor atoms bonded to the central atom). (a) The top view for the hexagonal single-layer structure, and (b) the cross view for the zinc-blend bulk structure.

The summations in the formula are over all neighbors j and k of atom i within a cutoff distance, $R + D$. Here, r_{ij} is the distance between atoms i and j, f^R is the repulsive potential energy function, f^A is the attractive potential energy function, and f^C is a smooth cutoff function that limits the range of the potential over the nearest-neighbor interactions. The a_{ij} and b_{ij} are many-body order parameters that determine the effect of atomic arrangements of neighboring atoms on the energy of the system. The $g(\theta_{ijk})$ is the bond angle between $i - j$ and $i - k$ pairs, as described in Fig. 1.

In this study, as recommended by Tersoff, the term a_{ij} is set to 1 ($\alpha = 0$). Therefore, four two-body terms, A, B, λ_1, λ_2 and six three-body terms λ_3, n, β, c, d, h are considered to be parameters values of which can be engineered to obtain desired physical characteristics. Also, in order to accurately describe the three-body interactions, particularly for the correct description of vacancy defect formation energies, X-N-N and N-X-X three-body interaction parameters are generated separately (first one is the center atom, second and third are the atoms bonded to the center atom).

The particle-swarm-optimization (PSO) algorithm as explained in our previous study [47] is used to generate the described 16 EIAP parameters for each material. For this purpose, the fitness function for the PSO is defined as

$$f\left(A, B, \lambda_1, \lambda_2, \lambda_3^X, n^X, \beta^X, c^X, d^X, h^X, \lambda_3^N, n^N, \beta^N, c^N, d^N, h^N\right)$$

$$= \sum_{j=1}^J \left(\frac{|d_j - a_j|}{d_j}\right). \tag{3}$$

where, d_j denotes the desired value of the characteristic j obtained by first-principles calculations, a_j denotes the actual value of the characteristic j obtained via empirical potential for a given set of parameters, and $J = 58$ is the total number of the certain physical characteristics of two crystal phases (hexagonal monolayers, h-BN, h-AlN,

and h-GaN and zinc-blend bulk structures, zb-BN, zb-AlN, and zb-GaN) to be optimized simultaneously. Here, the lattice constant (a_0), phonon frequencies (ω) corresponding to the selected acoustic and optic vibrations with different wavelengths, equation of states (EOS) defined as the deviation from the equilibrium energy via isotropic tensile and compressive strain, the formation energy difference between the h and zb crystal phases, and the formation energies corresponding to five different vacancy defect structures shown in the Supplemental Material [48] are considered. The values are determined by using the General Utility Lattice Program (GULP) code [49] throughout the EIAP-parameter-set optimization process.

The desired values of the variables are calculated via first-principles pseudopotential plane-wave simulations based on the density-functional theory (DFT) using the Vienna *ab initio* simulation package (VASP) [50–52]. In order to minimize the periodic layer interactions of the hexagonal structures, a vacuum spacing of 15 AA along the z direction is considered. A plane-wave basis set with 600- (700-) eV kinetic energy cutoff and the Γ point centered $24 \times 24 \times 1$ ($12 \times 12 \times 12$) k-point mesh within the Monkhorst-Pack scheme for the Brillouin-zone integration of the primitive cell are used for all the hexagonal monolayer (zinc-blend bulk) structures. In order to obtain the vibrational frequencies, the phonopy [53] code is employed by using the force constants computed from the density-functional perturbation theory [54] by means of VASP. For all the monolayer (bulk) structures, these calculations are carried out with $4 \times 4 \times 1$ ($3 \times 3 \times 3$) conventional supercell structure, considering the Γ centered $6 \times 6 \times 1$ ($4 \times 4 \times 4$) k-point grids for the Brillouin-zone sampling. The monovacancy, divacancy, and Stone-Wales defect formation energies are calculated as

$$E_f^{\mathrm{DFT}} = E_d - E_p + xE_X + nE_N, \quad (4)$$

where E_p, E_d, E_X, and E_N are the total energy of the perfect crystal structure, the energy of structure with defect, the ground-state energy of X elements, and the ground-state energy of N, respectively. x and n stands for the number of missing X, and N atoms, respectively.

The transport coefficients are calculated through CMD by using the Green-Kubo relations derived from the fluctuation dissipation theorem [55]. In the Green-Kubo method, the thermal conductivity that relates to the ensemble average of the heat-current autocorrelation function (HCACF) is given by

$$\kappa_{\alpha\alpha} = \frac{1}{Vk_BT^2} \int_0^\infty \langle J_\alpha(0)J_\alpha(t)\rangle dt, \quad (5)$$

where α represent the three Cartesian coordinates (x, y, and z directions), V is the volume of the simulation cell, k_B is the Boltzmann constant, T is the temperature of the system,

and $J_\alpha(t)$ is the heat current calculated as follows [56]:

$$\mathbf{J} = \sum_i \left(E_i\mathbf{v}_i + \frac{1}{2}\sum_{i<j}\left[\mathbf{F}_{ij}\cdot(\mathbf{v}_i+\mathbf{v}_j)\right]\mathbf{r}_{ij}\right), \quad (6)$$

where E_i is the total energy of the atom i, $\mathbf{v}_i$ is the velocity of atom i, $\mathbf{r}_{ij}$ denotes the interatomic distance between atoms i and j, and $\mathbf{F}_{ij}$ stands for the interatomic force.

The CMD simulations for thermal-transport analysis are performed using the Large-scale Atomic/Molecular Massively Parallel Simulator (LAMMPS) [57,58], with 1×10^6 time steps ($\Delta t = 0.5$ fs) in canonical ensemble (NVT) to reach the thermal equilibrium, and another 1×10^7 time steps in microcanonical ensemble (NVE) for heat-current calculations. Then, the mean HCACF, $[J_\alpha(0)J_\alpha(t)]_k$ is obtained using the calculated heat-current data by considering 500.000 time steps and 9.5×10^6 initial point, k with lags of increments of 10 time steps. In addition, the whole procedure is repeated for ten different sets of initial particle velocities randomly distributed by a Gaussian distribution as defined in LAMMPS. Next, averaging over ten different trials provide us with the overall average of HCACF, and the resulting figures are provided in the Supplemental Material [48] as examples. Finally, the data obtained as explained above are used to compute final lattice thermal conductivity with the following equations [55,59]:

$$\langle \mathbf{J}(0)\cdot\mathbf{J}(t)\rangle = A_1 e^{-t/\tau_1} + A_2 e^{-t/\tau_2}.$$

$$\kappa = \frac{1}{Vk_BT^2}\left(A_1\tau_1 + A_2\tau_2\right).$$

Here, τ_1 and τ_2 represent time constants, A_1 and A_2 represent the strength of phonon modes. The basic logic in the definition of two variables is to distinguish the contribution of short-range optical and long-range acoustic modes, which can make significant differences in thermal conductivity for some materials.

The CMD simulations for single-layer hexagonal structures are performed in quasisquare simulation cells, the width of which is approximately 81, 102, and 106 nm for BN, AlN, and GaN, respectively. And for zinc-blend and wurtzite structures simulations are performed in cubic cells with the edge length of approximately 16, 19, and 20 nm for BN, AlN, and GaN, respectively. In the volume calculation of the single-layer structures, we assume an effective layer thickness of 3.33 Å for monolayer h-BN, 3.4 Å for monolayer h-AlN, and 3.49 Å for monolayer h-GaN, in accordance with the results we obtain from the first-principles calculations of hexagonal bulk structures. In order to factor in the isotopic disorder nature of the crystals, the simulation cell structures contain randomly distributed 20% ^{10}B and 80% ^{11}B isotopes for BN, and 60% ^{69}Ga and 40% ^{71}Ga isotopes for GaN.

III. RESULTS

As previously mentioned, lattice constants, equation of states, phonon frequencies, defect energies and the difference of formation energies per atom of single-layer h and bulk zb crystal phases are included as physical characteristics in the potential fitting procedure. The Tersoff-type EIAP sets obtained using PSO are presented in Table I for BN, AlN, and GaN. In the Supplemental Material [48], the comparative results for all the physical quantities considered (first-principles results and the values obtained with the optimized potential parameters) are presented. The results show that the generated transferable EIAP set clearly represent the structural, mechanical, and dynamical properties of both h and zb structures of considered materials within a reasonable margin of error. Due to many possible unanticipated effects that may occur in the experimental fabrication procedures in different growth methods, yielding a material free from defect formations is highly improbable [60,61], in particular for monolayer structures [61–63]. Therefore, in order to obtain a parameter set well describing the characteristic of considered materials in the presence of defects, the monovacancy, bivacancy, and Stone-Wales defect [64,65] formation energies are factored in during the optimization procedure. The comparative results of the formation energies of five different vacancy defect structures created for the hexagonal single-layer phases of each material are presented in the Supplemental Material [48]. The listed energies are in very close agreement with first-principles calculations except for V_X and V_{X+3N} defects. Our definition of three-body parameter clearly worked well in distinguishing the V_X and V_N monovacancy formation energies.

Phonons are the primary heat carriers in semiconductors [66]. In order to fully grasp the thermal dependent properties of a material, an accurate characterization of the vibrational properties is essential. The phonon dispersion curves

obtained with EIAP sets are substantially compatible with the first-principles results as shown in Figs. 2(a)–2(f).

In addition, experimental data for h-BN [67] and zb-BN [68] structures have been added to phonon dispersions, and it is observed that the results of force-field-based calculations are in good agreement with measurement results. Notably, acoustic branches have a great coherence with the first-principles calculations for both monolayer and bulk phases of the BN, AlN, and GaN. In the first-principles phonon calculations, we do not include longitudinal and transverse optic mode splitting. Since we try to produce pair potential parameters, calculated errors in optic phonons are reasonable up to the deviation of the longitudinal-transverse optic splitting effect. On the other hand, the notable indirect effect of optical phonon modes on lattice thermal conductivity has been previously predicted for several different crystals including GaN [69–73], despite the relatively less direct contribution of these modes to κ compared with the acoustic ones [74,75]. Therefore, the noticeable difference in high-lying optic modes can be considered as the weakness of the generated parameter sets. However, our results presented below clearly show that the optical phonon representation of the generated EIAP parameters is good enough to get reasonable results for the thermal-transport properties of the considered crystals. Consequently, one can clearly conclude taking into account the comparisons that the generated pairwise transferable interatomic parameter sets accurately describe the desired physical properties of group-III nitrides.

Subsequent to the potential validation calculations, we predict the lattice thermal conductivity, $\kappa = (\kappa_{xx} + \kappa_{yy})/2$ of the monolayer BN, AlN, and GaN structures in the 200–700 K temperature range as shown in Fig. 3.

The κ of BN is observed to decrease from approximately 560 to approximately 120 $\mathrm{Wm^{-1}\,K^{-1}}$ between 200 and 700 K, and room-temperature value is calculated as

TABLE I.   Optimized Tersoff-type empirical interatomic potential parameters obtained by using the PSO method for BN, AlN, and GaN.

|	B-N	N-B	Al-N	N-Al	Ga-N	N-Ga
A (eV)	1205.446293	1205.446293	1258.567263	1258.567263	2249.391746	2249.391746
B (eV)	436.750025	436.750025	453.228512	453.228512	764.751142	764.751142
λ_1 (Å^{-1})	2.965635	2.965635	2.434869	2.434869	2.652624	2.652624
λ_2 (Å^{-1})	2.060658	2.060658	1.717680	1.717680	1.963739	1.963739
λ_3 (Å^{-1})	1.165721	1.108293	1.186759	1.100709	1.453060	1.166408
n	1.156834	0.939775	0.598233	1.220882	0.761872	1.070552
β	0.741928×10^{-6}	1.335243×10^{-6}	2.133047×10^{-6}	2.496023×10^{-6}	2.143554×10^{-6}	2.642801×10^{-6}
c	26320.215836	27483.938392	19110.741778	27568.039128	45996.528912	44736.208668
d	5.255691	7.783163	10.882090	8.292436	13.083985	12.497037
h	-0.870210	-0.749741	-0.972662	-0.816226	-0.990019	-0.693793
R (Å)	2.20	2.20	2.55	2.55	2.65	2.65
D (Å)	0.10	0.10	0.15	0.15	0.15	0.15
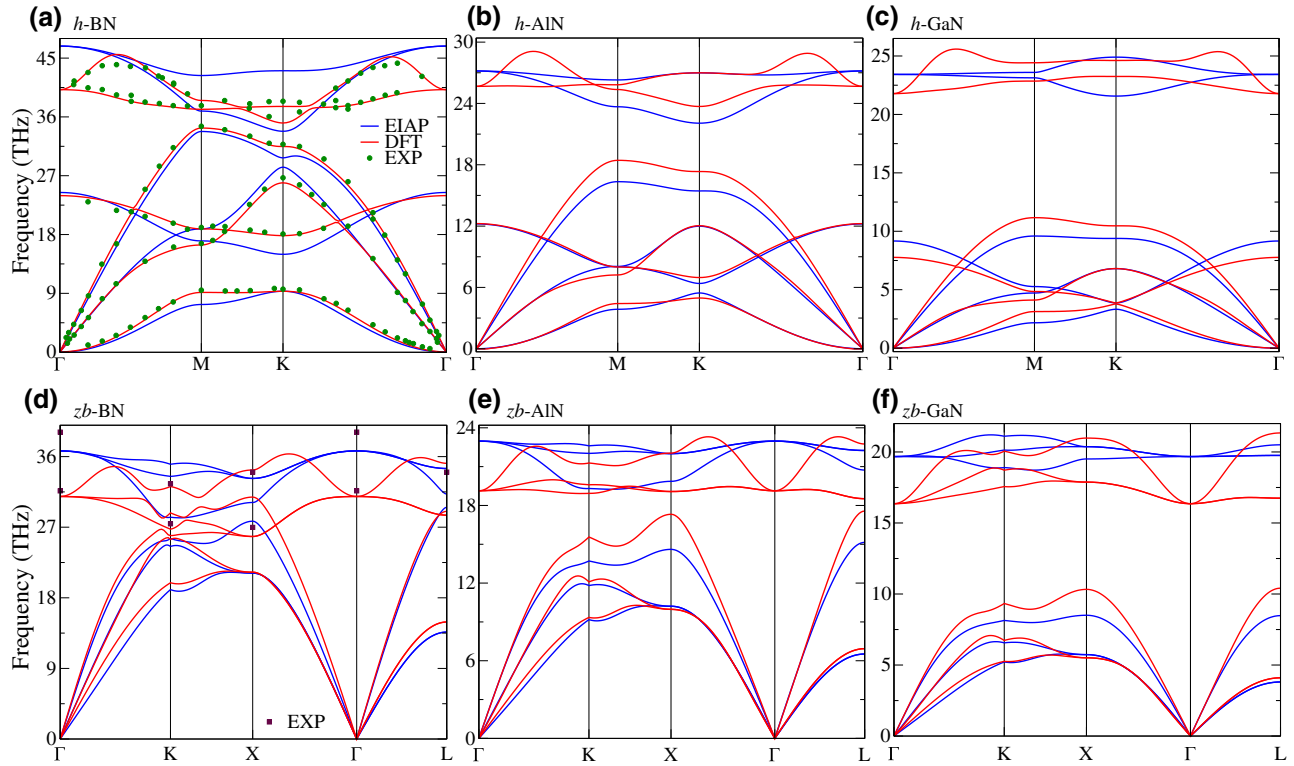
FIG. 2.   Phonon dispersions of the hexagonal monolayer (a) BN, (b) AlN, (c) GaN, and zinc-blende bulk (d) BN, (e) AlN, and (f) GaN along the high-symmetry reciprocal space points. The results of the first-principles (DFT, red line), force-field-based calculations (EIAP, blue line) and experimental data (green circle from Ref. [67], maroon square from Ref. [68]).

380 $Wm^{-1}K^{-1}$. These results are quite comparable with our previous prediction by nontransferable Tersoff potential [81]. We also investigate the effect of isotope disorder on κ and find out that the room-temperature κ of natural (with 20% ^{10}B and 80% ^{11}B) BN is obtained as 260 $Wm^{-1}K^{-1}$. The approximately 30% decrease on κ shows the strong influence of isotope disorder on thermal-transport properties of the material as previously predicted [76,82]. The room-temperature thermal conductivity for bulk h-BN is reported around 390 $Wm^{-1}K^{-1}$ by Sichel *et al.* [78]. Also, the room-temperature thermal conductivity values are calculated around 360 $Wm^{-1}K^{-1}$ for eleven-layer h-BN [79], 227–280 $Wm^{-1}K^{-1}$ for nine-layer h-BN [83], 250 $Wm^{-1}K^{-1}$ for five-layer h-BN [79], and 484 $Wm^{-1}K^{-1}$ for two-layer h-BN [80]. Moreover, Cai *et al.* recorded the thermal conductivity of one-, two-, and three-layer h-BN as 751, 646, and 602 $Wm^{-1}K^{-1}$, respectively, at close to room temperature using optothermal Raman measurements [84]. There is a notable deviation among the reported experimental results and calculations but the current picture may change with future studies. In fact, the strong influence of crystal disorders on measured lattice thermal conductivity values of low-dimensional systems and self-specific errors of used experimental thermal-transport characterization techniques in these measurements are explicit in the

literature as reviewed for graphene [85]. On the other hand, the underestimation of CMD simulation on κ is a well-known fact due to the collective excitation of phonon modes even at low temperatures [86]. However, the transferable potential parameter sets reported in this study, which enables simulation of a system consisting of up to a million atoms, clearly give reasonable results for the lattice thermal conductivity of these crystals.

For h-AlN, κ decreases from approximately 115 to 28 $Wm^{-1}K^{-1}$ within the same temperature range, while it is around 75 $Wm^{-1}K^{-1}$ at room temperature as seen in Fig. 3(b). Qin *et al.* [76] reported the room-temperature value as 74.43 $Wm^{-1}K^{-1}$ by means of first-principles-based solution of phonon Boltzmann transport equation (PBTE). Using the same thickness, we obtain κ as 82 $Wm^{-1}K^{-1}$, which is in quite good agreement.

The thermal conductivity of the h-GaN is observed to decrease from approximately 21 to 6 $Wm^{-1}K^{-1}$ in the 200–700 K temperature range as shown in Fig. 3(c). The calculated room-temperature value is predicted as 15 $Wm^{-1}K^{-1}$. This result is in conjunction with the first-principles-based PBTE solution reported in the literature [76,77,87,88], when the effective thickness values are selected in accordance with these studies. The percent abundance of Ga isotopes is as follows: 60% ^{69}Ga and 40% ^{71}Ga. Therefore, we investigate the effect of isotope
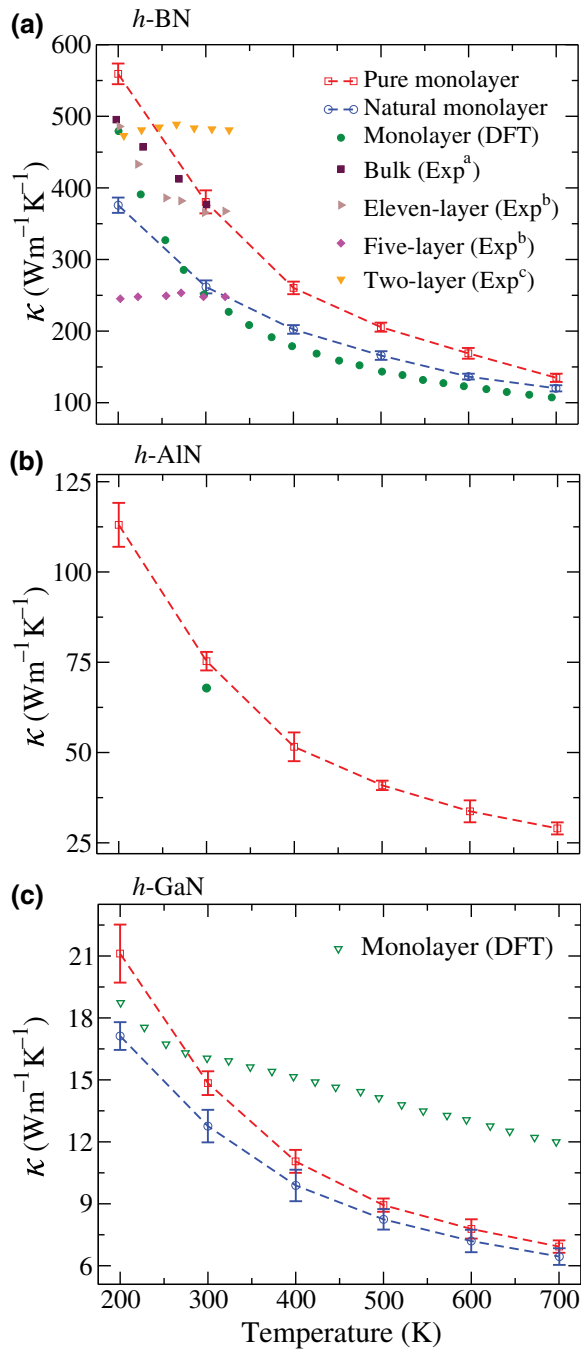
FIG. 3.   Calculated lattice thermal conductivity, κ for the isotopically pure (red dashed lines) and natural (blue dashed lines) hexagonal monolayer (a) BN, (b) AlN, (c) GaN crystals as a function of temperature. Theoretical literature data: monolayer (DFT) from Ref. [76] for BN and AlN, from Ref. [77] for GaN (for this data, effective layer thicknesses are normalized according to our study). Experimental data: a, b, c from Ref. [78–80], respectively.

disorder for also κ of GaN. Our results clearly depicted that the effect of isotope disorder is around 10%, mainly due to the fractional difference between the two isotope masses when compared with the *h*-BN.

The calculated room-temperature lattice thermal conductivity [$\kappa = (\kappa_x + \kappa_y + \kappa_z)/3$] values for the *zb* bulk phases are summarized in Fig. 4, as approximately 1350, 440, and 501 Wm^{-1} K^{-1} for *zb*-BN, *zb*-AlN, and *zb*-GaN, respectively. There is no experimental study on the thermal conductivity of the *zb*-AlN and *zb*-GaN in the literature. However, the measured room-temperature κ for *zb*-BN is 740 Wm^{-1} K^{-1} [89], which is almost half of the value calculated in this study, 1355 Wm^{-1} K^{-1} and the reported theoretical estimation, approximately 1300 Wm^{-1} K^{-1} [89,90]. But, when we factor in the isotope effect we practically get the same result as 764 Wm^{-1} K^{-1}. The reduction on the thermal conductivity with the isotope disorder is around 44% for the *zb*-BN, and surprisingly 48% for the *zb*-GaN.

In addition to the crystal structures considered in the optimization process, we also test the generated EIAP parameter sets on wurtzite (*wz*) crystal phases of the BN, AlN, and GaN. The accurate description of the generated potential for the desired physical properties can be clearly verified from the values presented in the Supplemental Material [48] in comparison with first-principles calculations. For instance, the calculated lattice constants are in agreement with first-principles data within a 10% margin of error. Also, the change in total energy via isotropic tensile and compression strain very well match with the first-principles-calculation results throughout the entire workspace. Figures 5(a)–5(c) present the comparative phonon frequencies calculated with the DFT and EIAP parameter sets of the *wz*-BN, -AlN, and, -GaN structures along high-symmetry directions of the Brillouin zone. Also the measurement results for *wz*-AlN [91] and -GaN [92] phases are presented in Figs. 5(b) and 5(c).
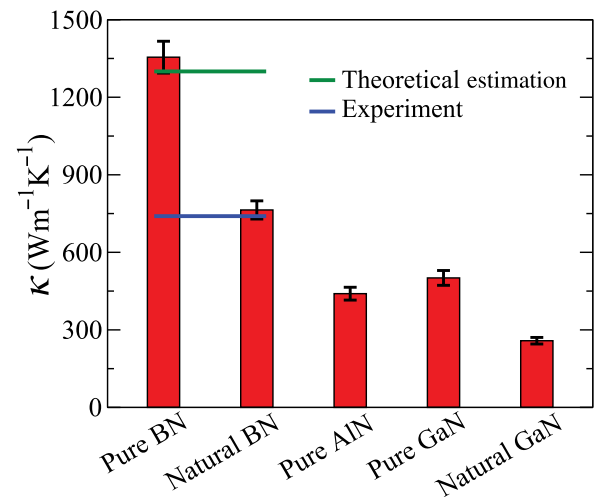

FIG. 4.   Calculated room-temperature lattice thermal conductivity, κ values for the isotopically pure and natural zinc-blend bulk BN, AlN, and GaN crystals. Here, the experimental data is from Ref. [89], the theoretical estimate is from Ref. [90].
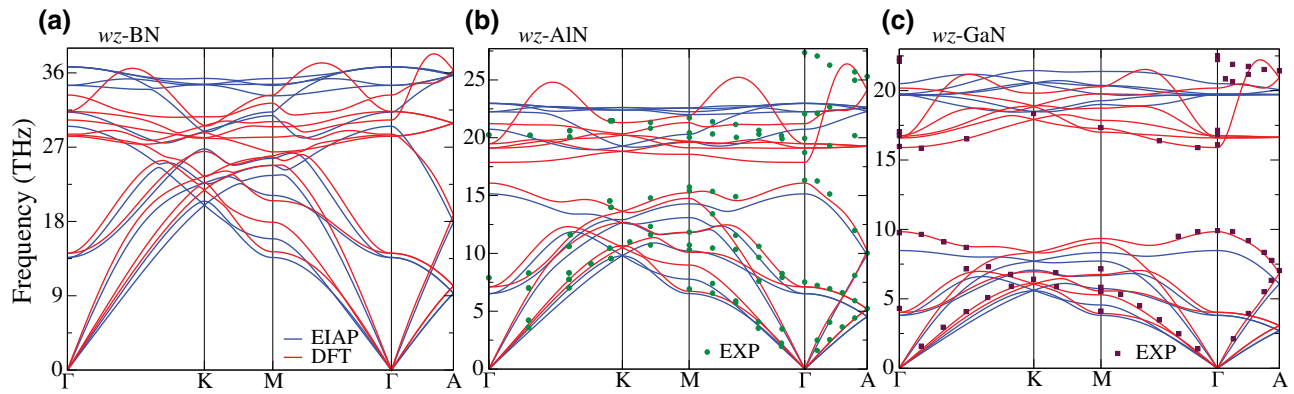
FIG. 5.   Phonon frequencies for the *wz* bulk (a) BN, (b) AlN, and (c) GaN along the high-symmetry directions of the Brillouin zone. The results of the first-principles (DFT, red line), force-field-based calculations (EIAP, blue line) and experimental data (green circle from Ref. [91], maroon square from Ref. [92]).

The results are quite consistent in particular for acoustic modes. Therefore, we can clearly claim that the transferable Tersoff potential parameters for the *wz*-BN, -AlN, and, -GaN structures are highly compatible with the results of the first-principles calculations, which is an important proof of the transferability of the EIAP parameters generated for the materials considered in this study.

The calculated lattice thermal conductivity for in-plane, $\kappa_{ip} = (\kappa_x + \kappa_y)/2$, and out-of-plane, $\kappa_{op} = \kappa_z$, directions of *wz* crystals are presented in Fig. 6.

The room-temperature values of κ are about 1040 (1190), 360 (370), and 275 (280) $Wm^{-1}K^{-1}$ for in-plane (out-of-plane) directions for pure *wz*-BN, -AlN, and -GaN, respectively. For *wz*-BN the results of the first-principles calculations recently reported by Chakraborty *et al.* [98], κ_{ip} (κ_{op}) = 1344 (1155) $Wm^{-1}K^{-1}$ are in parallel with our calculations. The measured κ of *wz*-AlN at room temperature is experimentally [89,90,93] estimated as 320 $Wm^{-1}K^{-1}$ (regardless of direction) and theoretically [89,99,100] reported as 285–400 $Wm^{-1}K^{-1}$, which are also consistent with our results. Recently, Xu *et al.* have experimentally measured the thermal conductivity of *wz*-AlN by the 3*w* method, and have obtained $\kappa = 237$ and $\kappa = 247$ $Wm^{-1}K^{-1}$ at room temperature for two samples [94]. In addition, the resulting κ_{ip}/κ_{op} ratio for AlN in our calculations, is 0.97 quite close to the value obtained by Li *et al.*, as 0.95 (the average value is around 300 $Wm^{-1}K^{-1}$). Several different experimental [89,90,93,95–97,101] and theoretical [37,87] studies report the average κ of *wz*-GaN between 170 and 260 $Wm^{-1}K^{-1}$, and 260 and 410 $Wm^{-1}K^{-1}$, respectively. The calculated κ value for GaN in this study is consistent with the reported results, however, the obtained $\kappa_{ip}/\kappa_{op} = 0.98$ ratio is higher than those reported in several different theoretical methods by Qin *et al.* [87], in which $\kappa_{ip}/\kappa_{op} = 0.8$–0.9. Another point to emphasize here is that the isotope disorder has a strong influence on thermal conductivity. The effect of the isotope dispersion on thermal conductivity is about 30% for *wz*-BN (730 and 807 $Wm^{-1}K^{-1}$ for in-plane and out-of-plane directions, respectively) and 8% for *wz*-GaN (253 and 259 $Wm^{-1}K^{-1}$ for in-plane and out-of-plane directions, respectively).

IV. CONCLUSION

In conclusion, we generate Tersoff-type transferable EIAP parameter sets for the BN, AlN, and GaN crystals using a stochastic optimization algorithm, particle-swarm optimization. The results clearly show that the generated parameters represent the structural, mechanical, and dynamical nature of all the tested crystal phases of nitride compounds considered with an acceptable level of accuracy, even for the *wz* crystals, which are not included explicitly in the optimization procedure. Therefore, the generated fully transferable EIAP parameter sets can be
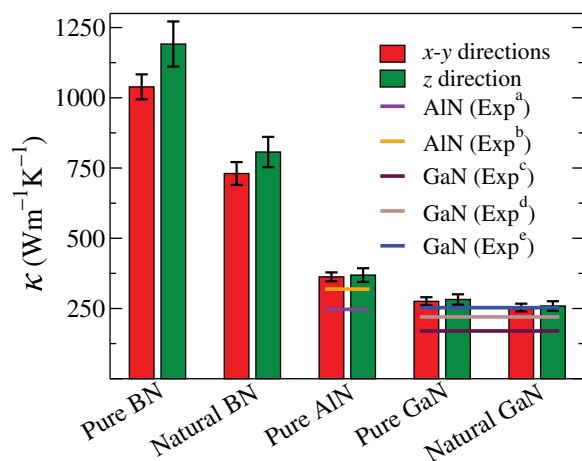

FIG. 6.   Calculated room-temperature lattice thermal conductivity values for the isotopically pure and natural wurtzite bulk BN, AlN, and GaN crystals. Here, experimental data a, b, c, d, e are from Ref. [93–97], respectively.

adopted to investigate the thermal properties of pristine and heterostructure bulk and nanosystems (except van der Waals heterostructures) even in the presence of isotope, vacancy, and grain boundary type of defects.

As we mention before, controlling and understanding energy dissipation and transport properties in nanostructure devices continue to be a rapid development and discovery area for more powerful, faster, and smaller device applications. In this context, we test the generated EIAPs via a systematic investigation of thermal-transport properties of well-known crystal structures of these compounds. Our results clearly demonstrate that our potential parameters reproduce the lattice thermal-transport properties of these systems with a high level of agreement with both theoretical and experimental studies reported in the literature. In addition, we predict a strong influence of isotope disorder on lattice thermal-transport properties of BN and GaN crystals, which clearly shows that disorder effects have to be taken into account in order to obtain more realistic results for materials and device systems.

ACKNOWLEDGMENTS

[1] S. Strite and H. Morkoç, GaN, AlN, and InN: A review, J. Vac. Sci. Technol. B **10**, 1237 (1992).

[2] O. Ambacher, Growth and applications of group III-nitrides, J. Phys. D: Appl. Phys. **31**, 2653 (1998).

[3] I. Vurgaftman, J. R. Meyer, and L. R. Ram-Mohan, Band parameters for III-V compound semiconductors and their alloys, J. Appl. Phys. **89**, 5815 (2001).

[4] I. Vurgaftman and J. R. Meyer, Band parameters for nitrogen-containing semiconductors, J. Appl. Phys. **94**, 3675 (2003).

[5] S. Nakamura, Nobel lecture: Background story of the invention of efficient blue InGaN light emitting diodes, Rev. Mod. Phys. **87**, 1139 (2015).

[6] R. Ferreyra, C. Zhu, A. Teke, and H. Morkoç, in *Group III Nitrides*, edited by S. Kasap and P. Capper, Springer Handbook of Electronic and Photonic Materials (Springer Handbooks. Springer, Cham, 2017).

[7] K. Miwa and A. Fukumoto, First-principles calculation of the structural, electronic, and vibrational properties of gallium nitride and aluminum nitride, Phys. Rev. B **48**, 7897 (1993).

[8] I. Gorczyca and N. Christensen, Band structure and high-pressure phase transition in GaN, AlN, InN and BN, Physica B: Condens. Matter **185**, 410 (1993).

[9] N. E. Christensen and I. Gorczyca, Optical and structural properties of III-V nitrides under pressure, Phys. Rev. B **50**, 4397 (1994).

[10] K. Kim, W. R. L. Lambrecht, and B. Segall, Elastic constants and related properties of tetrahedrally bonded BN, AlN, GaN, and InN, Phys. Rev. B **53**, 16310 (1996).

[11] R. J. Shul, A. J. Howard, S. J. Pearton, C. R. Abernathy, and C. B. Vartuli, High-densily etching of group III nitride ternary films, J. Electrochem. Soc. **143**, 3285 (1996).

[12] K. Shimada, T. Sota, and K. Suzuki, First-principles study on electronic and elastic properties of BN, AlN, and GaN, J. Appl. Phys. **84**, 4951 (1998).

[13] I. N. Przhevalskii, S. Y. Karpov, and Y. N. Makarov, Thermodynamic properties of group-III nitrides and related species, MRS Internet J. Nitride Semiconduc. Res. **3**, e30 (1998).

[14] J. Wu, When group-III nitrides go infrared: New properties and perspectives, J. Appl. Phys. **106**, 011101 (2009).

[15] S. Nakamura, M. Senoh, S.-i. Nagahama, N. Iwasa, T. Yamada, T. Matsushita, Y. Sugimoto, and H. Kiyoku, Room-temperature continuous-wave operation of InGaN multi-quantum-well-structure laser diodes with a long lifetime, Appl. Phys. Lett. **70**, 868 (1997).

[16] Y. Taniyasu, M. Kasu, and T. Makimoto, An aluminium nitride light-emitting diode with a wavelength of 210 nanometres, Nature **441**, 325 (2006).

[17] S. Mokkapati and C. Jagadish, III-V compound SC for optoelectronic devices, Mater. Today **12**, 22 (2009).

[18] N. Lu and I. Ferguson, III-nitrides for energy production: Photovoltaic and thermoelectric applications, Semicond. Sci. Technol. **28**, 074023 (2013).

[19] R. Jos, A semi-analytical, two-dimensional model for AlGaN/GaN high-electron-mobility-transistor Schottky currents at high reverse voltages, J. Appl. Phys. **114**, 074512 (2013).

[20] X. Li and X. Liu, Group III nitride nanomaterials for biosensing, Nanoscale **9**, 7320 (2017).

[21] C. L. Tsai, Y. Kobayashi, T. Akasaka, and M. Kasu, Molecular beam epitaxial growth of hexagonal boron nitride on Ni(111) substrate, J. Cryst. Growth **311**, 3054 (2009).

[22] L. Song, L. Ci, H. Lu, P. B. Sorokin, C. Jin, J. Ni, A. G. Kvashnin, D. G. Kvashnin, J. Lou, B. I. Yakobson, and P. M. Ajayan, Large scale growth and characterization of atomic hexagonal boron nitride layers, Nano Lett. **10**, 3209 (2010).

[23] S. Nakhaie, J. M. Wofford, T. Schumann, U. Jahn, M. Ramsteiner, M. Hanke, J. M. J. Lopes, and H. Riechert, Synthesis of atomically thin hexagonal boron nitride films on nickel foils by molecular beam epitaxy, Appl. Phys. Lett. **106**, 213108 (2015).

[24] A. A. Tonkikh, E. N. Voloshina, P. Werner, H. Blumtritt, B. Senkovskiy, G. Güntherodt, S. S. P. Parkin, and Y. S. Dedkov, Structural and electronic properties of epitaxial multilayer h-BN on Ni(111) for spintronics applications, Sci. Rep. **6**, 23547 (2016).

[25] T. Q. P. Vuong, G. Cassabois, P. Valvin, E. Rousseau, A. Summerfield, C. J. Mellor, Y. Cho, T. S. Cheng, J. D. Albar, L. Eaves, C. T. Foxon, P. H. Beton, S. V. Novikov, and B. Gil, Deep ultraviolet emission in hexagonal

boron nitride grown by high-temperature molecular beam epitaxy, 2D Mater. **4**, 021023 (2017).

[26] T. S. Cheng, A. Summerfield, C. J. Mellor, A. N. Khlobystov, L. Eaves, C. T. Foxon, P. H. Beton, and S. V. Novikov, High-temperature molecular beam epitaxy of hexagonal boron nitride with high active nitrogen fluxes, Materials **11**, 1119 (2018).

[27] P. Tsipas, S. Kassavetis, D. Tsoutsou, E. Xenogiannopoulou, E. Golias, S. A. Giamini, C. Grazianetti, D. Chiappe, A. Molle, M. Fanciulli, and A. Dimoulas, Evidence for graphite-like hexagonal AlN nanosheets epitaxially grown on single crystal Ag(111), Appl. Phys. Lett. **103**, 251605 (2013).

[28] V. Mansurov, T. Malin, Y. Galitsyn, and K. Zhuravlev, Graphene-like AlN layer formation on (111)Si surface by ammonia molecular beam epitaxy, J. Cryst. Growth **428**, 93 (2015).

[29] T. H. Seo, A. H. Park, S. Park, Y. H. Kim, G. H. Lee, M. J. Kim, M. S. Jeong, Y. H. Lee, Y.-B. Hahn, and E.-K. Suh, Direct growth of gan layer on carbon nanotube-graphene hybrid structure and its application for light emitting diodes, Sci. Rep. **5**, 7747 (2015).

[30] Z. Y. Al Balushi, K. Wang, R. K. Ghosh, R. A. Vilá, S. M. Eichfeld, J. D. Caldwell, X. Qin, Y.-C. Lin, P. A. DeSario, G. Stone, S. Subramanian, D. F. Paul, R. M. Wallace, S. Datta, J. M. Redwing, and J. A. Robinson, Two-dimensional gallium nitride realized via graphene encapsulation, Nat. Mater. **15**, 1166 (2016).

[31] H. Şahin, S. Cahangirov, M. Topsakal, E. Bekaroglu, E. Akturk, R. T. Senger, and S. Ciraci, Monolayer honeycomb structures of group-IV elements and III-V binary compounds: First-principles calculations, Phys. Rev. B **80**, 155453 (2009).

[32] H. Lu, Y. Guo, and J. Robertson, Chemical trends of Schottky barrier behavior on monolayer hexagonal B, Al, and Ga nitrides, J. Appl. Phys. **120**, 065302 (2016).

[33] Z. Huang, T.-Y. Lü, H.-Q. Wang, S.-W. Yang, and J.-C. Zheng, Electronic and thermoelectric properties of the group-III nitrides (BN, AlN and GaN) atomic sheets under biaxial strains, Comput. Mater. Sci. **130**, 232 (2017).

[34] D. Kecik, A. Onen, M. Konuk, E. Gürbü, F. Ersan, S. Cahangirov, E. Aktürk, E. Durgun, and S. Ciraci, Fundamentals, progress, and future directions of nitride-based semiconductors and their composites in two-dimensional limit: A first-principles perspective to recent synthesis, Appl. Phys. Rev. **5**, 011105 (2018).

[35] C. W. Chang, A. M. Fennimore, A. Afanasiev, D. Okawa, T. Ikuno, H. Garcia, D. Li, A. Majumdar, and A. Zettl, Isotope Effect on the Thermal Conductivity of Boron Nitride Nanotubes, Phys. Rev. Lett. **97**, 085901 (2006).

[36] L. Lindsay and D. A. Broido, Enhanced thermal conductivity and isotope effect in single-layer hexagonal boron nitride, Phys. Rev. B **84**, 155421 (2011).

[37] L. Lindsay, D. A. Broido, and T. L. Reinecke, Thermal Conductivity and Large Isotope Effect in GaN from First Principles, Phys. Rev. Lett. **109**, 095901 (2012).

[38] S. Thomas, K. M. Ajith, S. Chandra, and M. C. Valsakumar, Temperature dependent structural properties and

bending rigidity of pristine and defective hexagonal boron nitride, J. Phys.: Condens. Matter **27**, 315302 (2015).

[39] A. Tabarraei, Thermal conductivity of monolayer hexagonal boron nitride nanoribbons, Comput. Mater. Sci. **108**, 66 (2015).

[40] Y. Wu, Y. Xue, S. Qin, D. Liu, X. Wang, X. Hu, J. Li, X. Wang, Y. Bando, D. Golberg, Y. Chen, Y. Gogotsi, and W. Lei, Bn nanosheet/polymer films with highly anisotropic thermal conductivity for thermal management applications, ACS Appl. Mater. Interfaces **9**, 43163 (2017).

[41] C.-P. Feng, S.-S. Wan, W.-C. Wu, L. Bai, R.-Y. Bao, Z.-Y. Liu, M.-B. Yang, J. Chen, and W. Yang, Electrically insulating, layer structured SiR/GNPs/BN thermal management materials with enhanced thermal conductivity and breakdown voltage, Compos. Sci. Technol. **167**, 456 (2018).

[42] H. Song, J. Liu, B. Liu, J. Wu, H.-M. Cheng, and F. Kang, Two-dimensional materials for thermal management applications, Joule **2**, 442 (2018).

[43] D. Mandelli, W. Ouyang, O. Hod, and M. Urbakh, Negative Friction Coefficients in Superlubric Graphite–Hexagonal Boron Nitride Heterojunctions, Phys. Rev. Lett. **122**, 076102 (2019).

[44] S. Roosta, S. J. Nikkhah, M. Sabzali, and S. M. Hashemianzadeh, Molecular dynamics simulation study of boron-nitride nanotubes as a drug carrier: From encapsulation to releasing, RSC Adv. **6**, 9344 (2016).

[45] X.-K. Chen, J.-W. Hu, X.-J. Wu, P. Jia, Z.-H. Peng, and K.-Q. Chen, Tunable thermal rectification in graphene/hexagonal boron nitride hybrid structures, J. Phys. D: Appl. Phys. **51**, 085103 (2018).

[46] J. Tersoff, New empirical approach for the structure and energy of covalent systems, Phys. Rev. B **37**, 6991 (1988).

[47] A. Kandemir, H. Yapicioglu, A. Kinaci, T. Çağın, and C. Sevik, Thermal transport properties of MoS$_2$ and MoSe$_2$ monolayers, Nanotechnology **27**, 055703 (2016).

[48] See Supplemental Material at http://link.aps.org/supplemental/10.1103/PhysRevApplied.13.034027 for the comparison of structural properties, change in total energy with tensile and compressive strain and defect formation energies, obtained with generated potential and first-principles calculations, and the calculated heat-current autocorrelation functions using generated parameters.

[49] J. D. Gale and A. L. Rohl, The General Utility Lattice Program (GULP), Mol. Simul. **29**, 291 (2003).

[50] G. Kresse and J. Hafner, Ab initio molecular dynamics for liquid metals, Phys. Rev. B **47**, 558 (1993).

[51] P. E. Blöchl, Projector augmented-wave method, Phys. Rev. B **50**, 17953 (1994).

[52] G. Kresse and J. Furthmüller, Efficiency of ab-initio total energy calculations for metals and semiconductors using a plane-wave basis set, Comput. Mater. Sci. **6**, 15 (1996).

[53] A. Togo and I. Tanaka, First principles phonon calculations in materials science, Scr. Mater. **108**, 1 (2015).

[54] S. Baroni, S. de Gironcoli, A. Dal Corso, and P. Giannozzi, Phonons and related crystal properties from density-functional perturbation theory, Rev. Mod. Phys. **73**, 515 (2001).

[55] A. McGaughey and M. Kaviany, Thermal conductivity decomposition and analysis using molecular dynamics

simulations: Part II. Complex silica structures, Int. J. Heat Mass Transfer **47,** 1799 (2004).

[56] B. Mortazavi, L. F. C. Pereira, J.-W. Jiang, and T. Rabczuk, Modelling heat conduction in polycrystalline hexagonal boron-nitride films, Sci. Rep. **5,** 13228 (2015).

[57] S. Plimpton, Fast parallel algorithms for short-range molecular dynamics, J. Comput. Phys. **117,** 1 (1995).

[58] Lammps, http://lammps.sandia.gov.

[59] S. Nichenko and D. Staicu, Molecular dynamics study of the mixed oxide fuel thermal conductivity, J. Nucl. Mater. **439,** 93 (2013).

[60] R. Egerton, P. Li, and M. Malac, Radiation damage in the TEM and SEM, Micron **35,** 399 (2004).

[61] C. Jin, F. Lin, K. Suenaga, and S. Iijima, Fabrication of a Freestanding Boron Nitride Single Layer and its Defect Assignments, Phys. Rev. Lett. **102,** 195505 (2009).

[62] J. C. Meyer, A. Chuvilin, G. Algara-Siller, J. Biskupek, and U. Kaiser, Selective sputtering and atomic resolution imaging of atomically thin boron nitride membranes, Nano Lett. **9,** 2683 (2009).

[63] N. Alem, R. Erni, C. Kisielowski, M. D. Rossell, P. Hartel, B. Jiang, W. Gannett, and A. Zettl, Vacancy growth and migration dynamics in atomically thin hexagonal boron nitride under electron beam irradiation, Phys. Status Solidi RRL **5,** 295 (2011).

[64] D. G. Kvashnin, P. B. Sorokin, D. Shtansky, D. Golberg, and A. V. Krasheninnikov, Line and rotational defects in boron-nitrene: Structure, energetics, and dependence on mechanical strain from first-principles calculations, Phys. Status Solidi B **252,** 1725 (2015).

[65] S. Nahid, F. Hasan Bhuiyan, T. Rakib, and S. Mojumder, Effects of defects on the fracture strength of hexagonal boron nitride (2017).

[66] X. Gu, Y. Wei, X. Yin, B. Li, and R. Yang, Colloquium: Phononic thermal properties of two-dimensional materials, Rev. Mod. Phys. **90,** 041002 (2018).

[67] J. Serrano, A. Bosak, R. Arenal, M. Krisch, K. Watanabe, T. Taniguchi, H. Kanda, A. Rubio, and L. Wirtz, Vibrational Properties of Hexagonal Boron Nitride: Inelastic X-Ray Scattering and Ab Initio Calculations, Phys. Rev. Lett. **98,** 095503 (2007).

[68] S. Reich, A. C. Ferrari, R. Arenal, A. Loiseau, I. Bello, and J. Robertson, Resonant Raman scattering in cubic and hexagonal boron nitride, Phys. Rev. B **71,** 205201 (2005).

[69] D. A. Broido, M. Malorny, G. Birner, N. Mingo, and D. A. Stewart, Intrinsic lattice thermal conductivity of semiconductors from first principles, Appl. Phys. Lett. **91,** 231922 (2007).

[70] L. Lindsay and D. A. Broido, Three-phonon phase space and lattice thermal conductivity in semiconductors, J. Phys.: Condens. Matter **20,** 165209 (2008).

[71] J. An, A. Subedi, and D. Singh, Ab initio phonon dispersions for pbte, Solid State Commun. **148,** 417 (2008).

[72] Z. Tian, J. Garg, K. Esfarjani, T. Shiga, J. Shiomi, and G. Chen, Phonon conduction in PbSe, PbTe, and PbTe$_{1-x}$Se$_x$ from first-principles calculations, Phys. Rev. B **85,** 184303 (2012).

[73] O. Delaire, J. Ma, K. Marty, A. F. May, M. A. McGuire, M.-H. Du, D. J. Singh, A. Podlesnyak, G. Ehlers, M. D. Lumsden, and B. C. Sales, Giant anharmonic phonon scattering in PbTe, Nat. Mater. **10,** 614 (2011).

[74] J.-H. Zou and B.-Y. Cao, Phonon thermal properties of graphene on h-Bn from molecular dynamics simulations, Appl. Phys. Lett. **110,** 103106 (2017).

[75] L. Lindsay, D. A. Broido, and N. Mingo, Flexural phonons and thermal transport in graphene, Phys. Rev. B **82,** 115427 (2010).

[76] G. Qin, Z. Qin, H. Wang, and M. Hu, Lone-pair electrons induced anomalous enhancement of thermal transport in strained planar two-dimensional materials, Nano Energy **50,** 425 (2018).

[77] G. Qin, Z. Qin, H. Wang, and M. Hu, Anomalously temperature-dependent thermal conductivity of monolayer GaN with large deviations from the traditional $1/T$ law, Phys. Rev. B **95,** 195416 (2017).

[78] E. K. Sichel, R. E. Miller, M. S. Abrahams, and C. J. Buiocchi, Heat capacity and thermal conductivity of hexagonal pyrolytic boron nitride, Phys. Rev. B **13,** 4607 (1976).

[79] I. Jo, M. T. Pettes, J. Kim, K. Watanabe, T. Taniguchi, Z. Yao, and L. Shi, Thermal conductivity and phonon transport in suspended few-layer hexagonal boron nitride, Nano Lett. **13,** 550 (2013).

[80] C. Wang, J. Guo, L. Dong, A. Aiyiti, X. Xu, and B. Li, Superior thermal conductivity in suspended bilayer hexagonal boron nitride, Sci. Rep. **6,** 25334 (2016).

[81] C. Sevik, A. Kinaci, J. B. Haskins, and T. Çağın, Characterization of thermal transport in low-dimensional boron nitride nanostructures, Phys. Rev. B **84,** 085409 (2011).

[82] C. Sevik, A. Kinaci, J. B. Haskins, and T. Çağın, Influence of disorder on thermal transport properties of boron nitride nanostructures, Phys. Rev. B **86,** 075403 (2012).

[83] H. Zhou, J. Zhu, Z. Liu, Z. Yan, X. Fan, J. Lin, G. Wang, Q. Yan, T. Yu, P. M. Ajayan, and J. M. Tour, High thermal conductivity of suspended few-layer hexagonal boron nitride sheets, Nano Res. **7,** 1232 (2014).

[84] Q. Cai, D. Scullion, W. Gan, A. Falin, S. Zhang, K. Watanabe, T. Taniguchi, Y. Chen, E. J. G. Santos, and L. H. Li, High thermal conductivity of high-quality monolayer boron nitride and its thermal expansion, Sci. Adv. **5,** eaav0129 (2019).

[85] A. A. Balandin, Thermal properties of graphene and nanostructured carbon materials, Nat. Mater. **10,** 569 (2011).

[86] Z. Fan, L. F. C. Pereira, H.-Q. Wang, J.-C. Zheng, D. Donadio, and A. Harju, Force and heat current formulas for many-body potentials in molecular dynamics simulations with applications to thermal conductivity calculations, Phys. Rev. B **92,** 094301 (2015).

[87] Z. Qin, G. Qin, X. Zuo, Z. Xiong, and M. Hu, Orbitally driven low thermal conductivity of monolayer gallium nitride (GaN) with planar honeycomb structure: A comparative study, Nanoscale **9,** 4295 (2017).

[88] Y. Jiang, S. Cai, Y. Tao, Z. Wei, K. Bi, and Y. Chen, Phonon transport properties of bulk and monolayer GaN from first-principles calculations, Comput. Mater. Sci. **138,** 419 (2017).

[89] M. Levinshtein, S. Rumyantsev, and M. Shur, *Properties of Advanced Semiconductor Materials: GaN, AlN, InN,*

BN, SiC, SiGe (A Wiley-Interscience publication, Wiley, New York, 2001).

[90] G. Slack, Nonmetallic crystals with high thermal conductivity, J. Phys. Chem. Solids **34,** 321 (1973).

[91] M. Schwoerer-Böhning, A. T. Macrander, M. Pabst, and P. Pavone, Phonons in wurtzite aluminum nitride, Phys. Status Solidi B **215,** 177 (1999).

[92] T. Ruf, J. Serrano, M. Cardona, P. Pavone, M. Pabst, M. Krisch, M. D'Astuto, T. Suski, I. Grzegory, and M. Leszczynski, Phonon Dispersion Curves in Wurtzite-Structure *GaN* Determined by Inelastic X-Ray Scattering, Phys. Rev. Lett. **86,** 906 (2001).

[93] G. A. Slack, R. Tanzilli, R. Pohl, and J. Vandersande, The intrinsic thermal conductivity of AlN, J. Phys. Chem. Solids **48,** 641 (1987).

[94] R. L. Xu, M. Muñoz Rojo, S. M. Islam, A. Sood, B. Vareskic, A. Katre, N. Mingo, K. E. Goodson, H. G. Xing, D. Jena, and E. Pop, Thermal conductivity of crystalline AlN and the influence of atomic-scale defects, J. Appl. Phys. **126,** 185105 (2019).

[95] E. Sichel and J. Pankove, Thermal conductivity of GaN, 25–360 K, J. Phys. Chem. Solids **38,** 330 (1977).

[96] A. Jeżowski, B. Danilchenko, M. Boćkowski, I. Grzegory, S. Krukowski, T. Suski, and T. Paszkiewicz, Thermal conductivity of GaN crystals in 4.2–300 K range, Solid State Commun. **128,** 69 (2003).

[97] H. Shibata, Y. Waseda, H. Ohta, K. Kiyomi, K. Shimoyama, K. Fujito, H. Nagaoka, Y. Kagamitani, R. Simura, and T. Fukuda, High thermal conductivity of gallium nitride (GaN) crystals grown by HVPE process, Mater. Trans. **48,** 2782 (2007).

[98] P. Chakraborty, G. Xiong, L. Cao, and Y. Wang, Lattice thermal transport in superhard hexagonal diamond and wurtzite boron nitride: A comparative study with cubic diamond and cubic boron nitride, Carbon **139,** 85 (2018).

[99] W. Li and N. Mingo, Thermal conductivity of bulk and nanowire InAs, AlN, and BeO polymorphs from first principles, J. Appl. Phys. **114,** 183505 (2013).

[100] X. Mei Cai, Q. Neng Zhou, and J. Mei Wang, Comparison of two computing method on thermal conductivity of aluminum nitride, Adv. Mat. Res. **989–994,** 3509 (2014).

[101] D. I. Florescu, V. M. Asnin, F. H. Pollak, A. M. Jones, J. C. Ramer, M. J. Schurman, and I. Ferguson, Thermal conductivity of fully and partially coalesced lateral epitaxial overgrown GaN/sapphire (0001) by scanning thermal microscopy, Appl. Phys. Lett. **77,** 1464 (2000).

Correction: The previously published Figure 2(f) was incorrect and has been replaced.